ARTICLE

Reactivity of Pd-MO₂ encapsulated catalytic systems for CO oxidation

Received 00th October 2021, Accepted 00th January 20xx

DOI: 10.1039/x0xx00000x

Laura Paz Herrera,^a † Lucas Freitas de Lima e Freitas,^b † Jiyun Hong,^c Adam S. Hoffman,^c Simon R. Bare,^c Eranda Nikolla*^b and J. Will Medlin*^a

In this study, we present an investigation aimed at characterizing and understanding the synergistic interactions in encapsulated catalytic structures between the metal core (i.e., Pd) and oxide shell (i.e., TiO₂, ZrO₂, and CeO₂). Encapsulated catalysts were synthesized using a two-step procedure involving the initial colloidal synthesis of Pd nanoparticles (NPs) capped by various ligands and subsequent sol-gel encapsulation of the NPs with porous MO₂ (M=Ti, Zr, Ce) shells. The encapsulated catalytic systems displayed higher activity than the Pd/MO₂ supported structures due to unique physicochemical properties at the Pd-MO₂ interface. Pd@ZrO₂ exhibited the highest catalytic activity for CO oxidation. Results also suggested that the active sites in Pd encapsulated by an amorphous ZrO₂ shell structure were significantly more active than the crystalline oxide encapsulated structures at low temperatures. Furthermore, CO DRIFTS studies showed that Pd redispersion occurred under CO oxidation reaction conditions and as a function of the oxide shell composition, being observed in Pd@TiO₂ systems only, with potential formation of smaller NPs and oxide-supported Pd clusters after reaction. This investigation demonstrated that metal oxide composition and (in some cases) crystallinity play major roles in catalyst activity for encapsulated catalytic systems.

Introduction

Catalytic sites at metal-metal oxide interfaces have significant potential towards improving the activity or selectivity of technologically relevant catalytic processes. Accordingly, there has been significant effort toward synthesizing catalytic materials with different types of interfacial structures and characterizing the chemical properties of these interfaces with probe reactions. One of the most studied reactions is CO oxidation, which has important practical application for pollution abatement and is a useful model reaction system for investigations of new catalyst designs. 1-10 Vast literature exists on different catalytic systems that have been explored to increase conversion of CO oxidation at lower temperatures for energy optimization. One strategy involves generating a bifunctional interface between precious metals (for example, Pt, Au, and Pd) and metal oxide supports (for example, TiO₂, CeO₂, Co₃O₄, NiO, Al₂O₃, SiO₂ and ZrO₂).^{4,11-14} Among precious metals, Pd has shown promising activity.¹⁵ However, Pd nanoparticles (NPs) have poor stability¹⁶, and are prone to rapid agglomeration during catalytic conditions¹⁷, resulting in

significant loss of active catalytic centers and hence severe catalytic degradation¹⁸.

Several approaches, including the use of Pd-based bimetallic catalysts^{4,11,19} or incorporation of a secondary base metal^{20–22} have been proposed to stabilize Pd NPs. However, these systems are still limited by challenges related to the need for chemical^{23,24} and/or thermal treatments^{25,26}. Another approach for dispersing and stabilizing supported Pd NPs involves using surface-bound ligands.²⁷ However, the organic capping molecules generally decompose above 300 °C, and often limit the catalytic activities of the Pd NPs under 300 °C due to site blocking effects.²⁸ Several groups have demonstrated enhanced thermal stability of metal NPs using core-shell or encapsulated catalytic structures²⁹⁻³⁴. The encapsulation of Pd NPs by a porous oxide shell can minimize deactivation of the catalyst by sintering. 16 Metal oxide shells with either redox properties, such as $CeO_2^{18,29-31,35,36}$, ZrO_2^{37} and TiO_2^{37} , or with an inert nature, e.g., SiO₂^{28,38}, have been reported. In the former case, the metal-support interactions have been shown to lead to oxidation/reduction of the metal and the oxide,39 impacting catalytic performance. Furthermore, the 'active' lattice oxygen in the redox metal oxide shells was reported to facilitate oxidation of adsorbed CO.⁴⁰ The interface between noble metal NPs and redox metal oxide shells has been considered catalytically active for CO oxidation reaction. 17,41 Compared to the conventional supported catalysts, the encapsulated or encapsulated structures (metal NPs entrapped by a porous oxide shell) have been reported to exhibit higher activity, stability, and selectivity. 42,43 The proposed reasons for their superior catalytic properties include: (i) enhanced interfacial

Electronic Supplementary Information (ESI) available: [details of any supplementary information available should be included here]. See DOI: 10.1039/x0xx00000x

^a Department of Chemical and Biological Engineering, University of Colorado Boulder, Boulder, CO, USA 80303.

b. Department of Chemical Engineering and Materials Science, Wayne State University. Detroit. MI. USA 48202.

^c Stanford Synchrotron Radiation Lightsource, SLAC National Accelerator Laboratory, Menlo Park, CA, USA 94025.

[‡] These authors contributed equally to this article.

contact between the metal and the oxide; (ii) selectivity enhancement through reaction pathway control by the nanoporous oxide shell; and (iii) enhanced metal NP stability through trapping within the metal oxide nanostructures, improving sintering resistance. Conversely, non-reducible metal oxide shells have mainly been linked to stabilization of metal NPs as their sole function. 18

In this work, we have investigated Pd NPs encapsulated with various MO_2 porous shells (i.e., TiO_2 , CeO_2 , and ZrO_2). A combination of X-ray absorption spectroscopy (XAS) with surface-sensitive techniques, such as DRIFTS, was used to understand and describe the structure and chemistry of the catalysts' reactive surface. Furthermore, kinetic studies using CO oxidation as a probe reaction allowed for performance and stability testing of the various $Pd-MO_2$ systems. These findings provide insights into metal-support interfacial interactions of encapsulated catalysts for industrially relevant applications.

Experimental

Synthetic procedures

Synthesis of Pd NPs. Using our previously reported method,⁴⁴ Pd⁰ particles were synthesized using 9 mL of oleylamine (OAm) and 1 mL of trioctylphosphine (TOP), as reducing and surface stabilizing agents, and 0.1 g of precursor ((Pd(acac)₂) for 1 hour at 220 °C. To extract the NPs, an excess amount of ethanol was added, followed by centrifugation. The resulting Pd_{TOP} NPs were redispersed in chloroform (5 mL) for the next steps in the synthesis and further characterization. Monodispersed Pd NPs were also synthesized using polyethylene glycol (PEG) as reducing and surface stabilizing agent^{45,46}. Specifically, 4 g of PEG with 2000 molecular weight was used to reduce Pd(II) ions from the 67.7 mg of precursor ((Pd(acac)₂) to Pd⁰ metal at 120 °C for two hours. The reaction product was collected by adding an excess amount of DI water, followed by centrifugation at room temperature. The resulting Pd_{PEG} NPs were redispersed in DI water (3 mL) for the next steps in the synthesis and further characterization.

Synthesis of CeO₂ precursor. Ceric tetrakis(octyloxide) was synthesized using a previously reported protocol in the literature^{31,47,48}. Specifically, 5.48 g of ammonium cerium(IV) nitrate were dissolved in 20 mL of dried methanol under an inert atmosphere. 6.4 mL of dried n-octanol was added under vigorous stirring at room temperature, followed by the dropwise addition of 10.0 mL of sodium methoxide solution. Immediately after, gaseous NH₃ and a bright yellow precipitate (Ce(OCH₃)₄) were formed. 25 mL of dried toluene was then added, and the mixture was heated to 50 °C for 8 hours. Methanol was completely removed from the reaction mixture by distillation of the system at 73 °C under Ar for 15 hours. This step was followed by the addition of 25 mL of dried toluene and stirring at 50 °C for an additional 2 hours. The formed NaNO₃ was removed from the mixture by centrifugation and washed using toluene. Finally, toluene was removed by distillation at 40 °C under reduced pressure for 24 hours, resulting in an oil product with a deep orange color.

Synthesis of Pd@MO2 encapsulated catalytic structures. A modified sol-gel approach was used for the encapsulation of Pd NPs, as previously reported⁴⁴. The first step in the synthesis involved the modification of Pd_{TOP} NPs surface using cetyl trimethylammonium bromide (CTAB). Initially, 22 g of CTAB was dissolved in 100 mL of dried ethanol (reaction media) under magnetic stirring. Presynthesized Pd_{TOP} NPs were suspended in chloroform (5 mL) by sonication and then added into the CTAB/ethanol solution dropwise. In the case of the hydrophilic NPs (Pd_{PEG} NPs), the appropriate amount of Pd NPs was suspended in DI water (1 mL) by sonication and then added dropwise into the reaction media (100 mL of dried ethanol) under magnetic stirring. The mixture was then heated to 45 °C for 20 min under vigorous stirring to disperse the Pd NPs, followed by cooling to room temperature. The sol-gel process started by injecting the MO₂ precursor (titanium(IV) butoxide, zirconium(IV) n-propoxide, or ceric tetrakis (octyloxide)) using a syringe pump with an injection rate of 6.7 µL/sec. The reaction was performed for 24 hours, and the product was collected by centrifugation and washed three times using a 1:1 by volume methanol:water solution. The collected particles were then dried at 80 °C overnight before further characterizations.

Synthesis of Pd NPs supported on porous MO₂ as control catalysts.

The preparation of the control catalysts started with the synthesis of Pd_{TOP} NPs under the same condition as the Pd_{TOP} NPs in the encapsulated catalytic structures. Prior to the synthesis of TiO₂ films, surface modification of the Pd NPs with surfactant molecules (CTAB) was performed following the same procedure as discussed in the last topic. The surface-modified Pd NPs were dispersed in ethanol prior to sequential impregnation on the porous MO₂ support. The preparation of the porous MO₂ (i.e., TiO₂) support started with heating the reaction media (100 mL of dried ethanol) to 45 °C for 20 min. After the solution was cooled to room temperature, the MO₂ precursor (titanium(IV) butoxide) was injected precisely the same way as in the case of encapsulated catalytic systems. The reaction was performed for 24 hours or until completion. The product was collected by centrifugation and washed three times using a 1:1 by volume methanol:water solution. The collected particles were then dried at 80 °C overnight. The last step involved the sequential impregnation of the Pd NPs dispersed in DI water onto the porous MO2 support. The powder was dried at 80 °C overnight before further characterization.

Characterization Techniques

Powder X-ray diffraction (PRXD). Powder X-ray diffractometry (PXRD) analysis was performed using a Bruker Phaser II X-ray diffractometer with Cu K α radiation of 1.5418 Å.

High-resolution transmission electron microscopy (TEM). High-resolution transmission electron microscopy (TEM) studies were conducted using a JEOL 2010 transmission electron microscope operated at 200 kV. The TEM grids for all the

samples were prepared using the same procedure. Ten microliters of the redispersed Pd NPs in water or hexane were diluted with 5 mL methanol (for the hydrophilic ligands) or hexane (for the hydrophobic ligands), respectively, and sonicated for 20 minutes before dropwise deposition onto a Cu grid. The histogram of the Pd NPs size was measured by counting the diameter of 100 NPs in 3 random areas. ImageJ software was used to process the TEM micrographs.

High-resolution scanning transmission electron microscopy (STEM). High-angle annular dark-field (HAADF)-STEM micrographs were obtained using a Talos F200X electron microscope (Thermo Fisher Scientific, USA) equipped with a field emission electron source at an acceleration voltage of 200 keV. Further, energy dispersive X-ray spectroscopy (EDS) mapping was performed using Talos F200X electron microscope equipped with Super-X EDS consisting of four windowless silicon drift (SDD) detectors (area of each detector: 30 mm²) to aid in high sensitivity during elemental analysis.

Diffuse reflectance infrared Fourier transform spectroscopy (DRIFTS). CO-DRIFTS studies on Pd@MO2 were performed to gain insights into structural properties and types of CO adsorption sites on the encapsulated catalytic systems. These experiments were conducted using a Thermo Scientific Nicolet 6700 FT-IR, where a closed cell was used to hold the sample for analysis. The cell consisted of a chamber with a sample cup holder, a heating system with a thermocouple, two ports for the inlet and outlet of gas, and a dome with IR windows. The CO DRIFTS characterization experiments included a pretreatment at controlled gas compositions and temperatures, followed by dosing the sample with CO, and the final purging step in Ar while spectra were collected for 20 minutes. The sample was first pretreated at 400 °C or 250 °C (sample dependent) in an oxidative environment under flowing 20% O2 in Ar for an hour, with a subsequent reductive step at 200 °C under flowing 20% H₂ in Ar for an hour, and a final purge under flowing Ar at 200 °C for 30 minutes. The temperature was then decreased to 50 °C, and CO was dosed on the surface of the sample for 20 minutes under flowing 10% CO in Ar. Finally, CO was purged under flowing Ar and spectra were collected continuously for 20 minutes. The spectrum collected at 5 minutes was used for comparison amongst different samples.

Nitrogen physisorption. The pore size distribution of the synthesized catalysts was determined via nitrogen physisorption experiments in a Micromeritics ASAP 2020 system, using a non-local density functional theory (NLDFT) method.^{49,50} All the samples were degassed at 150 °C for 24 hours before a typical microporous structure analysis was conducted by Micromeritics ASAP 2020. The NLDFT method was based on a cylindrical, porous oxide surface model, using a nonnegative regularization value of 0.1 for smoothing.

Inductively coupled plasma—mass spectrometry (ICP-MS). The content of Pd in the reported catalysts was determined via inductively coupled plasma—mass spectrometry (ICP-MS), using an Agilent 7700x ICP-MS system with an indium solution (10 ppb) as an internal standard. The catalyst was digested using a

stainless-steel autoclave (Parr Instrument Company) with a 2:1 volume mixture of nitric acid (67-70%, Sigma-Aldrich) and hydrogen peroxide solution (30 wt.%, Sigma-Aldrich) at 215 $^{\circ}$ C for 4 hours. This was followed by dilution with 2% nitric acid solution.

In-situ X-ray absorption spectroscopy (XAS). In-situ X-ray absorption spectroscopy (XAS) measurements were carried out at beamline 9-3 at the Stanford Synchrotron Radiation Lightsource (SSRL) at SLAC National Accelerator Laboratory. Experiments were performed at the Pd K-edge (calibrated using metallic Pd at 24350.0 eV) using fluorescence yield with a PIPS detector. For each sample/condition, four X-ray absorption near edge structure (XANES) spectra were collected and merged to improve the signal-to-noise ratio. The catalyst powder was packed into a capillary flow reactor and placed at 45° to the incident beam in an in-situ cell.51 Initially, the catalyst was exposed to a 25 mL min⁻¹ flow of He at room temperature. After that, the catalyst was pretreated in 20% O₂ in He at 400 °C for 1 hour and 20% H₂ in He at 200 °C for 1 hour. The pretreatment was followed by purging under He at 200 °C for 30 minutes. CO oxidation reaction was performed during heating from room temperature to 350 °C. Post-reaction analysis was performed at room temperature under He and 10% H₂ in He flow. The X-ray absorption spectra were normalized and analyzed using Athena in the Demeter software package.52

Linear combination fitting analysis (LCF). Linear combination fitting (LCF) analysis was performed with Athena software of Demeter package⁵². For each sample spectrum, the analysis was done within an energy range of -30 eV below to +40 eV above the edge using bulk Pd and PdO standard spectra as weighted components. During each fit, the standards were constrained to have no EO shift, and the weights were forced to be between 0 and 1, while not constrained to a weight sum of 1.

H₂/D₂ scrambling. A tubular packed-bed gas phase reactor coupled with a mass spectrometer was employed to carry out H₂/D₂ exchange experiments, which were used to estimate the availability of surface metal active sites. For each catalyst, the exchange activity was measured before pretreatment, after RP-M (moderate-temperature oxidative-reductive pretreatment), and after RP-H (high-temperature oxidative-reductive pretreatment). A flow rate of 20 vol.% H₂ in Ar was kept at 40 mL min⁻¹. Three injections of 0.2 mL pure D₂ were introduced through the bypass for calibration, followed by three injections through the catalyst bed to measure HD formation rates. The D_2 conversion was used for estimation of the forward H_2/D_2 scrambling rates, given that H₂ was in great excess. Control experiments on large quantities of a 5 wt.% Pd supported commercial catalyst (Pd/Al₂O₃) allowed for the estimation of the equilibrium conversion, which was found to be >95%. For this reason, measurements for all rates were conducted at D₂ conversions below 50%, and the reverse reaction corresponding to HD dissociation was neglected. To estimate apparent dispersions, H₂/D₂ exchange rates were measured, at a conversion of 50%, for the control supported Pd catalyst with a

ARTICLE

known dispersion of 42% (obtained from CO chemisorption⁵³). These measurements were extrapolated to estimate the quantity of exposed surface Pd atoms for all catalysts, which was then used to calculate percent dispersion and metal surface area. Note that this method for estimating percent dispersion is fairly accurate for all catalysts at H_2/D_2 scrambling activity of ~50% conversion, given that calculations are referenced to the performance of the control catalyst at 50% conversion. However, dispersion values could be overestimated for catalysts with reactivity far below 50% conversion.

Catalytic Reactivity Studies

Gas-phase reactor studies were carried out to determine the reactivity of the encapsulated catalytic structures for CO oxidation reaction. A mass spectrometer was used to analyze the composition of the outlet stream based on the mass fragments of the gases and determine the formation of CO₂ as a function of temperature. The packed bed reactor was prepared by packing the catalyst powder in between two layers of glass wool, with flow through the catalyst. For consistency and comparison purposes, the total Pd metal loading into the reactor was kept at 0.09 mg for all experiments. The gas flow rates were set to ensure control over catalytic conversion for the reaction temperatures in the ranges of interest. All the reactivity testing experiments consisted of an initial pretreatment followed by three cycles of CO oxidation reaction. The catalyst was pretreated at 250 °C or 400 °C in an oxidative environment under flowing $20\%\ O_2$ in He for an hour, then reduced for an hour at 200 °C under flowing 20% H_2 in He, and finally purged for 30 minutes under flowing He at 200 °C. The temperature was then decreased to 30 °C, and a total 50 sccm flow rate of a 1: 10: 39 mixture of CO: O2: He was fed to the reactor. The first CO oxidation temperature ramp was carried out by increasing the temperature at 10 °C/min to 350 °C, dwelling for 5 minutes, and lowering back to room temperature (RT). Two more ramps were carried out identical to the first ramp, with two hours of dwelling at RT in between each ramp. Reactivity analysis was performed by calculating the percent conversion based on the highest and lowest intensity signal obtained for CO₂ production as a function of temperature. Then, light-off curves were prepared, and the conversion was plotted against temperature for all three ramps. The light-off temperature was set to be that at which the catalyst achieved a 50% conversion of CO into CO_2 . The CO conversion (X_{CO}) was calculated by recording the CO_2 signal (m/z = 44). The lowest CO_2 signal obtained prior to reaction was used as a baseline, representing 0% conversion. Using the levelled-off CO_2 intensity at high temperature as the value corresponding to 100% conversion, the CO_2 intensity signal obtained at each data point was compared to the baseline to obtain the percent conversion.

Results and discussion

Encapsulated versus Supported Catalytic Structures for Pd-TiO₂ System: Characterization and Catalytic Performance

Hydrophilic Pd NPs were synthesized using two different methods. In the first method, Pd NPs were directly synthesized using trioctylphospine (TOP) and oleylamine (OAm) as surface stabilizing and reducing agents, respectively, and their surfaces were modified with hexadecyltrimethylammonium bromide (CTAB) to make the NP surfaces hydrophilic prior to encapsulation or impregnation onto MO2, as previously reported⁵⁴. The second approach was based on a polyol method involving polyethylene glycol (PEG) as a surface stabilizing and reducing agent⁴⁶. In this case, no further modification of the NP surface was needed prior to encapsulation due to the hydrophilic nature of the surface ligands. The encapsulation of the Pd NPs involved a controlled sol-gel approach, as detailed in the Experimental Section.33 The same Pd NPs were also supported on porous oxide films of TiO2 (synthesized using the same sol-gel technique as for encapsulation) using sequential impregnation. Transmission electron micrographs (TEMs) of Pd NPs capped with the various ligands are shown in Figure S1. The characteristics of the different catalysts are summarized in Table 1. Pd NPs obtained by the two methods described above display different metal particle sizes. When Pd NPs were synthesized using TOP/OAm, the average metal particle diameter was 1.99 ± 0.64 nm, while in the case of PEG, the average Pd NP diameter was reduced to 1.28 ± 0.91 nm. The difference in the size of the NPs could be due to the reaction temperature needed to reduce the Pd precursor using the different agents (220 °C for TOP/OAm vs. 120 °C for PEG). The Pd loading of the samples was determined by ICP-MS, as shown in Table 1. It can be observed that the Pd content resulting from the two preparation methods ranged from 0.05 wt.% for Pd_{PEG}@TiO₂ to 0.2 wt.% for Pd_{TOP}@TiO₂. The different Pd loading for the Pd_{PEG}@MO₂ could be due to the possible weak intermolecular attractive forces induced by the long chain (steric hindrance) of the surface-bound ligand of Pd NPs (PEG) with the oxide precursor during synthesis.

Table 1 Characterization of the catalysts after RP-M pretreatment.

Sample	Name Pd load	ding ^a , % BET Surface Ar	ea ^b , m ² × g ⁻¹ Total Volume in Po	ores ^b , cm ³ × g ⁻¹ Light off at T ₅₀ ^c , °C
Pd _{TOP} /	TiO ₂ 0.153 :	± 0.014 318 ±	4 0.20	288 ± 7
Pd _{TOP} @	TiO ₂ 0.159 :	± 0.006 306 ±	1 0.20	255 ± 7
Pd _{PEG} @	OTiO ₂ 0.048 :	± 0.002 309 ±	3 0.21	. 227 ± 2
Pd _{PEG} @	CeO ₂ 0.437 :	± 0.054 94 ±	2 0.06	234 ± 1
Pd _{PEG} @	ZrO ₂ 0.450 :	± 0.026 163 ±	3 0.12	194 ± 5

^aDetermined by ICP-MS. Three runs were taken for each sample to obtain the standard deviation.

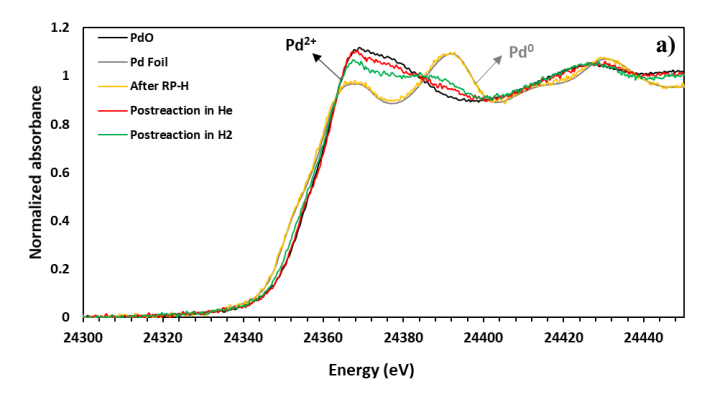
 $^{{}^{\}text{b}}\text{Obtained using N}_2$ physisorption.

^cUncertainties indicate standard deviation of T₅₀ values for three temperature ramps.

Prior to catalytic testing, the as-synthesized catalysts were exposed to a moderate temperature redox pretreatment (RP-M), involving oxidative treatment with 20% O₂/He at 250 °C for 1 hr, followed by a reductive treatment with 20% H₂/He at 250 °C for 1 hr, with a final purging step in pure He at 250 °C for 30 mins. The purpose of the pretreatment was to clean the catalyst's surface of residual organic species from synthesis and assure Pd reduction prior to catalytic testing. Catalyst characterization following this treatment using X-ray diffraction (XRD) showed that the oxide shell exhibited a tetragonal crystallographic structure corresponding to anatase TiO₂ (Figure S2). Nitrogen physisorption studies (Figure S3) showed that all catalysts exhibited type IV isotherms⁵⁵ with a uniform microporous structure (insert, Figure S2). All Pd-TiO₂ catalysts exhibited BET surface areas in the range 300-320 m² g⁻¹ (Table 1). The prepared catalysts were evaluated for CO oxidation using a heating rate of 10 °C/min from room temperature to 350 °C. Table 1 and Figure S4 show the light-off temperatures (T₅₀) and curves, respectively, for CO oxidation on encapsulated (Pd_{PEG}@TiO₂, Pd_{TOP}@TiO₂) and supported (Pd_{TOP}/TiO₂) catalystsThe light-off temperature (T₅₀) was defined as the temperature at which a conversion of 50% was achieved for each catalytic system; shifts in this temperature help assess catalyst performance. Based on the light-off temperatures, Table 1 shows that the performance of encapsulated catalytic structures containing Pd NPs capped with TOP (Pd_{TOP}@TiO₂) was lower than that for the encapsulated structure containing Pd NPs capped with PEG (Pd_{PEG}@TiO₂). One potential reason for this could be the effect of RP-M pretreatment conditions at 250 °C in the removal of Pd surface ligands (PEG versus TOP/OAm). PEG decomposes at >160 °C, which should lead to its complete removal during pretreatment, while TOP requires temperatures above 300 °C for complete removal.^{28,56,57} This suggests that TOP could potentially act as a Pd site blocker during CO oxidation leading to the lower activity of $Pd_{TOP}@TiO_2$ catalyst⁵⁸. When comparing encapsulated versus supported catalyst systems, Table 1 shows that encapsulated structures performed better than the control conventional supported catalysts (i.e., Pd_{TOP}/TiO₂), likely due to the enhanced interface between Pd and TiO2 and/or limited agglomeration of the Pd NPs under reaction conditions.

In-situ XAS and CO-DRIFTS studies on Pd@TiO₂ System

To determine the oxidation state of Pd NPs in encapsulated catalytic structures, XAS studies were carried out on Pd_{PEG}@TiO₂, the catalyst with the best performance for CO oxidation. After placing the catalyst in a quartz-capillary-based microreactor, XAS spectra were recorded continuously under He flow. Prior to analysis, the catalyst was pretreated using a high-temperature redox pretreatment (RP-H) involving an oxidative step at 400 °C followed by a reductive treatment at 200 °C to ensure the complete removal of carbonaceous species from the exposed catalyst surface. To quantitively analyze the fraction of Pd oxidation states, linear combination fitting (LCF) of the normalized Pd K-edge XANES spectra was performed, taking PdO and Pd metal foil as reference compounds representing Pd²⁺ and Pd⁰, respectively. Excellent quality fits



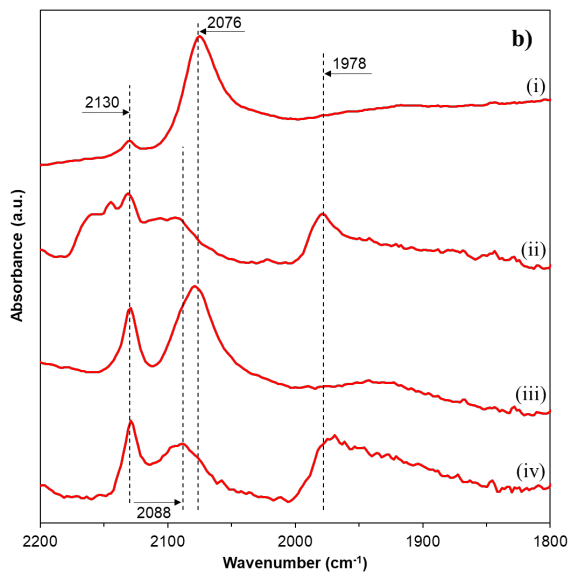


Figure 1 a) XANES spectra of Pd_{PEG} TiO₂ before and after CO oxidation; b) CO DRIFTS spectra of 0.048 wt.% Pd_{PEG} TiO₂ obtained during minute 5 of CO purge in Ar (i) before in-situ CO oxidation reaction, (ii) after in-situ reaction, and (iii) after in-situ reaction with further RP-H redox treatment. The spectrum (iv) corresponds to spectra of 0.048 wt.% Pd_{PEG} TiO₂ obtained at 5 min of CO purge in Ar after ex-situ CO oxidation reaction in a gas-phase reactor. All spectra were collected post-exposure to gas-phase CO at 50 °C.

were obtained using a fit range of -30 to 40 eV (E_0), with agreement factors around 0.0015. Phase composition analysis, yielding the fraction of Pd²⁺ and Pd⁰ within the sample in different stages is shown in Table S1. The Pd K-edge XANES spectra in Figure 1a shows that the catalysts were reduced to almost Pd⁰ - 99% of phase composition - during the RP-H pretreatment. Operando XANES Pd K-edge spectra measured during CO oxidation are shown in Figure S5. As the temperature and CO conversion increased, the absorption Pd K-edge shifted to lower energy, and the intensity of the "white line" increased. This suggests partial oxidation caused by coverage of the Pd surface with adsorbed oxygen species after depletion of CO (which, at low temperatures is chemisorbed more strongly on Pd sites than oxygen and prevents the latter from oxidizing the Pd sites).⁵⁹ After CO oxidation and postreaction exposure to He, the Pd K-edge spectra resembled that of PdO, indicating mainly oxidic Pd species, as shown in Figure 1a. It is established that the K-edge threshold energy shifts higher as the formal oxidation state of the X-ray absorbing atom increases.60 Qualitatively, an increase in the oxidation state of the catalyst is

associated with an increase the K-edge energy. Upon introduction of 10% H₂, the Pd K-edge spectrum suggests a mixture of Pd⁰ and Pd²⁺ states of the catalyst with a resultant phase composition of 35% and 65%, respectively, visible as an increase in the intensity of the XANES white line for the Pd_{PEG} @ TiO_2 – indicating the reduction of the PdO phase to Pd⁰. XANES studies were also performed for Pd_{TOP}@TiO₂. The variations in the oxidation state of Pd in the Pd_{TOP} @TiO₂ catalyst under different gaseous environments are plotted in Figure S6. After the pretreatment, Pd NPs were predominantly metallic within 86% of Pd⁰ obtained from LCF. Interestingly, under CO oxidation conditions, Pd remained mainly in a metallic state in Pd_{TOP}@TiO₂, unlike Pd_{PEG}@TiO₂ which exhibited a higher extent of oxidation of Pd. Evaluating quantitatively the obtained data by LCF showed that Pd species in Pd_{TOP}@TiO₂ became largely reduced (91%) after reaction. On the other hand, Pd_{PEG}@TiO₂ postreaction in He shows that 86% of Pd species are oxidized during reaction. After reaction and under H₂ flow, a Pd hydride phase formation was observed, consistent with its metallic nature. On-line fluent gas analysis from the XAS in-situ reactor using a mass spectrometer (Figure S7) showed that CO conversion as a function of temperature was in good agreement with the obtained trends from conventional packed bed reactor studies, highlighting the higher catalytic activity of Pd_{PEG}@TiO₂ vs. Pd_{TOP}@TiO₂. The differences in the oxidation state between the $Pd_{PEG}@TiO_2$ and $Pd_{TOP}@TiO_2$ observed in XAS could be due to the presence of surface ligands on Pd in the case of Pd_{TOP}@TiO₂ keeping the surface reduced and minimizing interaction with the reactive species. These results suggest that oxidic Pd sites are associated with catalytic turnover for CO oxidation. This is in agreement with the literature report which showed that Pd2+ coordinated with a redox support promoted CO adsorption leading to its reduction to Pd+ by CO61, which is also supported by our CO Fourier transform spectroscopy (DRIFTS) studies discussed below.

To probe the nature of the active surface structure under reaction conditions for Pd_{PEG}@TiO₂, CO DRIFTS studies were performed (Figure 1b). Spectra were collected for 20 minutes during the purging of CO from the surface of the catalysts in He, which was performed before reaction (spectrum (i)), after insitu reaction (spectrum (ii)), after in-situ reaction followed by RP-H redox pretreatment at 400 °C (spectrum (iii)), and after exsitu reaction performed in a gas-phase reactor with further RP-H treatment (spectrum (iv)). A prominent peak centered at 2076 cm⁻¹ appeared after the initial RP-H treatment prior to reaction, along with a sharp peak at 2130 cm⁻¹, as observed in the top spectrum (i), Figure 1b. Both peaks resided in a region corresponding to linearly bound CO on Pd, where the 2076 cm⁻ ¹ peak is ascribed to atop CO on Pd⁰, and the peak at 2130 cm⁻¹ corresponds to atop CO on Pd+.62 Interestingly, the peak centered at 2130 cm⁻¹ was observed consistently throughout the experiment, both before and after in-situ reaction, but its intensity relative to the 2076 cm⁻¹ peak varied. The changes in relative intensity of the two major peaks under CO oxidation conditions could be explained by the fact that before reaction, the catalyst was mostly reduced and Pd was in a metallic state, in accordance with the prominent peak at 2076 cm⁻¹. However,

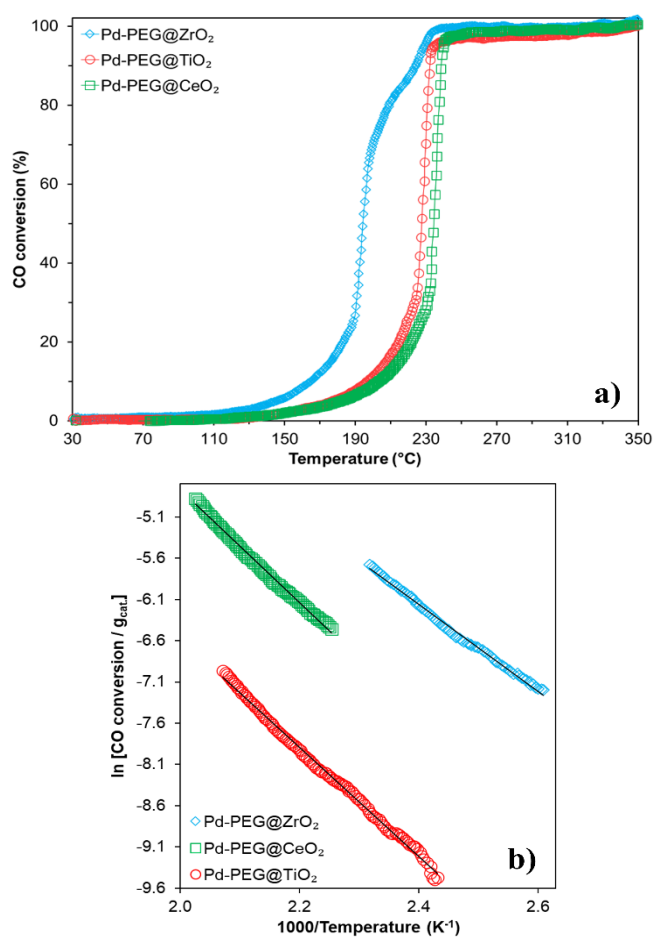


Figure 2 Catalytic properties of (red) $Pd_{PEG}@TiO_2$, (green) $Pd_{PEG}@CeO_2$, and (blue) $Pd_{PEG}@ZrO_2$. a) CO conversion for CO oxidation; b) Arrhenius plot for CO oxidation reactions over $Pd_{PEG}@TiO_2$, $Pd_{PEG}@CeO_2$, and $Pd_{PEG}@ZrO_2$.

as the catalyst was exposed to oxygen and CO during in-situ CO oxidation at 350 °C, Pd NPs redispersed into smaller Pd clusters and into oxidized Pd in the form of Pd+, as suggested by the increase in the intensity of the peak at 2130 cm-1 relative to 2076 cm⁻¹ observed in spectrum (iii). In the presence of CO at 350 °C, formation of Pd-CO bonds can lead to the weakening in the binding strength of Pd to TiO2, resulting in Pd atoms becoming mobile on the surface and redispersing into oxidized Pd species. 63-66 As observed in spectrum (ii), immediately after in-situ CO oxidation, a peak centered at 1978 cm⁻¹ emerged, corresponding to bridge-bound CO on Pd+, further supporting redispersion of Pd during CO oxidation.^{67,68} In spectrum (iv), collected after ex-situ reaction, both peaks corresponding to linearly bound CO on Pd emerged at 2130 cm⁻¹ and 2076 cm⁻¹, along with a peak for bridge-bound CO on Pd at 1978 cm⁻¹. Interestingly, peaks similar in location and intensity emerged after in-situ and ex-situ CO oxidation reaction, as observed in spectra (iii) and (iv) of Figure 1b.

Effects of the oxide (MO₂) shell composition on CO oxidation for Pd@MO₂ systems

Reducible oxides such as CeO₂ and TiO₂ have shown to exhibit a positive effect on the activity of supported Pd catalysts toward

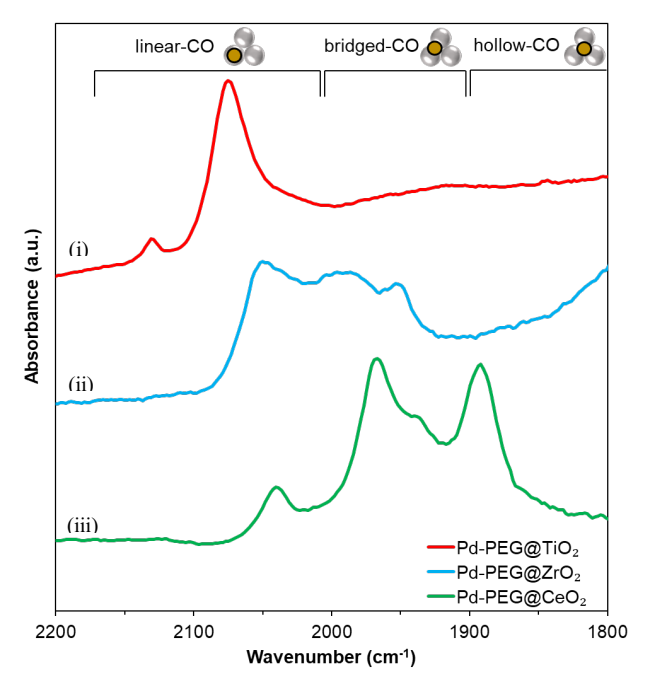


Figure 3 CO DRIFTS spectra of (i) Pd_{PEG}@TiO₂, (ii) Pd_{PEG}@ZrO₂, and (iii) Pd_{PEG}@CeO₂ obtained during minute 5 of CO purge in Ar before in-situ CO oxidation reaction.

CO oxidation due to the redox properties of the metal oxide at the Pd-MO interface.¹⁷ However, zirconia (ZrO₂), an oxide that requires much higher temperatures to reduce, has also shown promise when used as support for Pd. The enhanced performance of this system has been attributed to rapid oxygen exchange between the Pd surface and ZrO₂, which was found to be faster than the exchange between the metal surface and the gas phase.⁶⁹ Given this understanding, Pd NPs with the best performance (Pd_{PEG} NPs), were encapsulated with various oxide shells ($MO_2 = TiO_2$, CeO_2 , and ZrO_2) to determine their effect on the catalytic activity for CO oxidation. After the RP-M treatment, amorphous ZrO₂, tetragonal anatase TiO₂, and cubic cerianite CeO_2 were obtained for $Pd_{PEG}@ZrO_{2-amorphous}$, Pd_{PEG}@TiO₂, and Pd_{PEG}@CeO₂, respectively (Figure S2). To gain insight into the porous structure of the TiO2, CeO2, and ZrO2 shells, N₂ physisorption studies were used. The BET surface area and total pore volumes, as shown in Table 1, were different for the various metal oxide shells. The pore size distribution (Figure S3) was narrow and centered at about 3.7, 2.4, and 2.4 nm for TiO₂, CeO₂, and ZrO₂-based catalysts, respectively. ICP results showed that the Pd loading achieved after synthesis for systems with TiO₂, CeO₂, and ZrO₂, were 0.048 wt.%, 0.44 wt.%, and 0.45 wt.%, respectively.

The performance tests were carried out on all encapsulated catalytic systems and the metal oxides themselves for comparison. Reactivity was normalized by Pd metal loading into the reactor, which was kept consistent at 0.09 mg for all experiments to compensate for any differences in the Pd loading on the various Pd@MO₂ catalysts. As observed in Figure 2a, the reactivity of the catalysts for CO oxidation, measured under identical testing conditions, varied depending on the nature of the MO₂ shell for encapsulated structures. Apparent activation energy (E_a^{app}) values were obtained using

an Arrhenius-type plot, as shown in Figure 2b. Table S2 shows that the calculated E_a^{app} close to 44 kJ mol⁻¹ for Pd_{PEG}@ZrO₂, lower than that of ~55 kJ mol-1 for Pd_{PEG}@TiO₂, or ~57 kJ mol-1 for Pd_{PEG}@CeO₂, consistent with the activity trends reported in Figure 2a. This difference in reactivity among Pd@MO₂ catalysts is potentially associated with differences in the CO oxidation mechanism on these systems. Over Pd@TiO2, based on the studies above and literature on supported Pd/TiO₂ systems¹⁷, the reaction was hypothesized to proceed through a surface reaction between the weakly adsorbed CO and oxygen via a Langmuir-Hinshelwood mechanism. For Pd/CeO2 catalyst, however, the reaction mechanism has been reported to involve oxygen activation at different sites; CO adsorbed on Pd species was shown to interact with surface lattice oxygen of CeO2 or oxygen ions activated by the anion vacancies near Ce3+.70 In the case of Pd@ZrO₂, a redox or Mars van Krevelen mechanism has been suggested in the literature.69 Table 1 shows that Pd_{PEG}@ZrO₂ exhibited the lowest light-off temperature for CO oxidation of 194 °C, compared to Pd_{PEG}@TiO₂ (227 °C) and Pd_{PEG}@CeO₂ (234 °C). Previous reports highlighted oxygen mobility at the interface between the metal and ZrO₂ assisting in the Mars van Krevelen mechanism for CO oxidation as the potential reason for the enhanced activity of the Pd-ZrO₂ system.71-74

CO DRIFT spectra were collected for all three Pd_{PEG}@MO catalysts after RP-H treatment and prior to CO oxidation reaction, using the procedure previously described in the Experimental Section, to shed light on the catalyst active surface structure. Figure 3 shows that the location of the observed major peaks varied depending on the metal oxide used for Pd NP encapsulation. In the case of the Pd_{PEG}@TiO₂ (spectrum (i), Figure 3), two major sharp vibrational peaks were observed in the 2000-2150 cm⁻¹ range, characteristic of CO binding linearly to Pd in the form of CO-Pd+ and CO-Pd0. Contrastingly, in the case of Pd_{PEG}@ZrO₂, a broad peak extending from 1920-2080 cm⁻¹ and composed of three overlapping peaks, was observed (spectrum (ii), Figure 3), and ascribed to linearly bound CO on Pdo, bridge-bound CO on Pdo, and bridge-bound CO on Pd(100).62,75 These results suggest that Pd species in Pd_{PEG}@ZrO₂ before reaction were completely reduced, with CO binding preferentially to metallic Pd sites. In the case of Pd_{PEG}@CeO₂ (spectrum (iii), Figure 3), two sharp peaks, one in the region corresponding to bridge-bound CO to Pd⁰ and one ascribed to CO bound onto hollow metallic Pd sites were observed, along with a small peak in the region ascribed to linearly bound CO to Pdo. The variations in peak location, shape, and relative intensities observed between the three spectra prior to in-situ CO oxidation reaction indicate that the nature of the metal oxide shell and its interfacial interaction with Pd plays an important role in the formation of different types of active sites, which could potentially impact the generation of distinct catalytic properties and reactivity for each Pd@MO system, as observed in Figure 2a. To further shed light on the changes in the reactive surface of the Pd@MO₂ catalysts during reaction, an extended study was performed where insitu CO oxidation reaction was conducted and DRIFTS scans during CO purging in Ar were collected, as shown in Figures S8

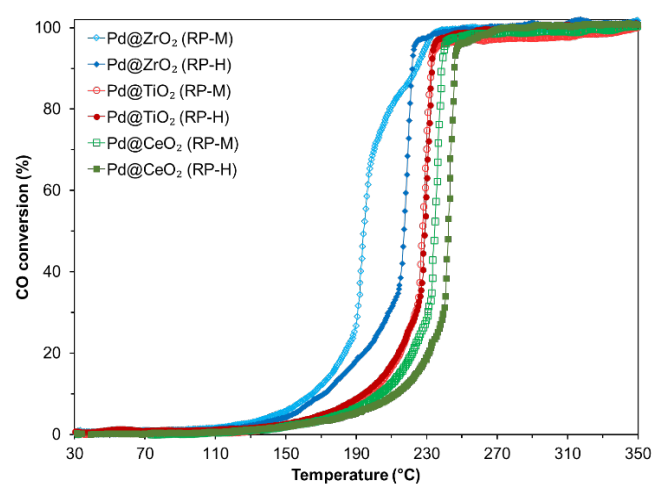


Figure 4 Light-off CO conversion curves for CO oxidation of $Pd_{PEG}@ZrO_2$, $Pd_{PEG}@TiO_2$ and $Pd_{PEG}@CeO_2$ at RP-M (moderate-temperature oxidative pretreatment at 250 °C followed by reduction at 250 °C) and RP-H (high-temperature oxidative pretreatment at 400 °C followed by reduction at 200 °C) conditions.

(carbonyl region, 1800-2200 cm⁻¹) and S9 (full spectra, 1200-2400 cm⁻¹). Peaks in the 1200-1600 cm⁻¹ region (Figure S9) correspond to carbonate species bound to the metal oxide (OCO vibrations). Spectra (i) and (ii) for Pd_{PEG}@TiO₂ in Figure S8 show two peaks emerging at 2076 and 2130 cm⁻¹, corresponding to linearly bound CO to Pd⁰ and Pd⁺, respectively. As previously discussed, the changes in the relative intensity of 2130 to 2076 cm⁻¹ also observed in Figure 1 before and after reaction suggest Pd redispersion, which could impact the reactivity of the catalyst for CO oxidation. In the case of Pd_{PEG}@ZrO₂, changes were observed in the metal carbonyl region (1800-2200 cm⁻¹, Figure S8) before (spectrum (iii)) and after (spectrum (iv)) in-situ CO oxidation reaction. As previously shown in spectrum (ii) of Figure 3, three bands appeared prior to reaction, centered at 1952, 1994, and 2042 cm⁻¹. After being exposed to reaction conditions, the three peaks shifted and formed two major peaks centered at 1970 and 2035 cm⁻¹, corresponding to a-top bound and bridge bound CO on Pdo, respectively.⁶² The obtained CO DRIFTS results for Pd_{PEG}@ZrO₂ indicate that the rapid oxygen exchange between the Pd surface and ZrO₂ during reaction resulted in similar availability of metal sites and similar CO-Pd interactions, but slightly different CO-ZrO₂ interactions postreaction. Conversely, spectra (v) and (vi) in Figure S8 for Pd_{PEG}@CeO₂ before and after CO oxidation reaction, respectively, indicate that no significant changes occurred in the reactive surface of this catalyst after reaction. The intensity and location of all bands observed both in the metal-carbonyl region (1800-2200 cm⁻¹) and in the region corresponding to interactions between CO and CeO₂ (1400-1600 cm⁻¹, Figure S9) remained essentially the same before (spectrum (i)) and after CO oxidation reaction (spectrum (ii)). These observations suggest that the bridge and hollow binding of CO to Pd remain unaffected despite being exposed to reaction conditions for CO oxidation.

Figure 4 shows the effect of the RP-M and RP-H redox pretreatment on the catalytic structure and activity of the $Pd@MO_2$ materials toward CO oxidation. As observed in Figure S2, ZrO_2 was the only metal oxide shell studied that remained

amorphous under a pretreatment temperature of 250 °C, and thus it was subjected to treatments at various temperatures until a tetragonal crystallographic structure was achieved at 400 °C to assess the effect of crystallinity on the catalytic activity. For consistency, all three Pd@MO systems were subjected to the same RP-H pretreatment, and the results obtained were then compared to those obtained from the experiments using the RP-M treatment. The temperature of reduction for these experiments was kept at 200 °C to avoid the possibility of inducing strong metal-support interaction (SMSI) effects, which could block Pd sites. 76,77 Figure S10 shows the HAAD STEM images and EDS mapping of Pd@MO2 (M= Ti, Ce, or Zr) structures. The ZrO₂-based catalyst was characterized using XRD, as reported in Figure S11. It was confirmed that after the RP-H treatment, the Pd_{PEG}@ZrO₂ had achieved a crystalline structure, and all samples exhibited a degree of pore closure and loss of surface area upon pretreatment. The light-off curves shown in Figure 4 were obtained with both the RP-M and RP-H pretreated catalysts and used to compare variations in the reactivity of each Pd@MO2 system as a function of the pretreatment oxidation temperature conditions to determine the impact of crystallinity of MO₂ on the performance of the catalysts.

As observed in Figure 4 and reported in Table S2, the light-off temperature, representative of the catalytic reactivity, of the Pd_{PEG}@CeO₂ system (green curves) slightly increased (by < 10°C) as the temperature of the oxidative treatment was increased. Similarly, the differences in activity were analyzed for the Pd_{PEG}@TiO₂ system (red curves) as a function of pretreatment temperature. Figure 4 shows that the activity of Pd_{PEG}@TiO₂, analyzed in terms of the light-off temperature and the shape of the light-off curve, remained unchanged regardless of the temperature of pretreatment applied prior to reaction. The insignificant changes in the CO oxidation reactivity for both Pd_{PEG}@TiO₂ and Pd_{PEG}@CeO₂ systems as a function of pretreatment temperature were consistent with the fact that crystallinity of the oxide shell was the same at both pretreatment temperatures. Conversely, in the case of Pd_{PEG}@ZrO₂ (blue curves), the light-off temperature increased about 20 °C when the oxidative pretreatment temperature was increased via the RP-H treatment. As observed in Figure 4, the shape of the curve corresponding to the RP-M pretreated catalyst, Pd_{PEG}@ZrO_{2-amorphous}, exhibited variations as a result of pretreatment temperature, particularly above 50% CO conversion. To ensure that no additional structural changes occurred during reaction, six temperature ramps were conducted on selected materials for catalytic recyclability testing and no major changes were noted after the 3rd cycle. Thus, three temperature ramps were conducted on all catalysts investigated in this work. Given that a crystalline ZrO2 shell was only formed after subjecting the catalyst to the RP-H treatment, the shape of the curve corresponding to the RP-H treated Pd_{PEG}@ZrO₂, indicated an improvement in the thermal stability of the catalyst. Moreover, it can be observed in Figure 4 that the Pd_{PEG}@ZrO₂ (RP-H treated) catalyst achieved complete conversion at the lowest temperature. Overall, independent of the pretreatment temperature, $Pd_{PEG}@ZrO_2$ system exhibited the best performance for CO oxidation.

H₂/D₂ scrambling experiments were performed as a characterization technique to determine HD exchange rates and estimate dispersions before pretreatment, after RP-M, and after RP-H for the Pd_{PEG}@ZrO₂, Pd_{PEG}@TiO₂, and Pd_{PEG}@CeO₂ catalysts. Dispersion here is used as a measure of the fractional exposed metal surface area and is determined by calculating the ratio of surface metal atoms by the total number of metal atoms. As observed in Figure S12 and as reported in Table S3, a clear trend is observed for all three catalysts, where scrambling activity (and hence active surface area) is higher after RP-H and is lower when no pretreatment is performed, suggesting that oxidative-reductive pretreatments increase the availability of exposed Pd active sites. Estimated dispersion was similar for all three catalysts after RP-H, as observed in Figure S12, whereas the activity prior to pretreatment was much higher for Pd_{PEG}@ZrO₂ than that for Pd_{PEG}@CeO₂. Interestingly, after RP-M, the trend is reversed, with a higher apparent active surface area observed for Pd_{PEG}@CeO₂, suggesting that the increased availability of Pd active sites observed after pretreatment is affected by the nature of the metal oxide used for encapsulation. These findings support our claim that variations in the reactivity of encapsulated catalysts arise from changes in the Pd-MO interactions. Moreover, it can be concluded that the trend observed for reactivity of encapsulated catalysts for CO oxidation after RP-H, where Pd_{PEG}@ZrO₂ is the most active catalyst, is due to the interaction between Pd and ZrO₂, given that the exposed available Pd site density is nearly the same for all encapsulating oxides.

Although Pd_{PEG}@ZrO_{2-amorphous} showed the best overall catalytic performance, the light-off temperature for Pd_{PEG}@ZrO₂ was still lower than those obtained with both Pd_{PEG}@CeO₂ and Pd_{PEG}@TiO₂ catalytic systems. These results suggest that Pd_{PEG}@ZrO₂ provides the best encapsulated catalytic system for CO oxidation, independent of the crystallinity of the oxide shell. The exceptional low-temperature catalytic activity observed for metal encapsulated in amorphous ZrO2, poses a promising material for further investigation for industrially relevant reactions that allow preservation of the amorphous structure. Two factors have been reported as the main contributors to the enhancement of catalytic activity for CO oxidation on supported Pd catalysts: (i) the dynamic reducibility of Pd²⁺ to Pd⁰, and (ii) the participation of lattice oxygen of the redox oxide support.⁷⁸ We propose that the Pd-ZrO₂ interface leads to improved CO oxidation catalytic activity because: (i) ZrO₂ reduces when in close contact with Pd; (ii) metal-metal oxide interactions between Pd and ZrO₂ enhance PdO stability; and (iii) the equilibrium oxidation-reduction properties of the Pd@ZrO2 core-shell catalysts are not a simple sum of those expected for the individual PdO-Pd and ZrO₂ phases.⁷⁹ Contact between the transition metal and ZrO₂ in encapsulated structures also provides opportunities unavailable with CeO2 and TiO2-based catalysts due to the fact that ZrO₂ does not form a stable reduced phase under normal conditions.

Conclusions

Pd-MO₂ encapsulated catalytic systems were prepared by a two-step protocol. The encapsulated catalytic systems displayed higher activity and stability when compared to the control-supported Pd/MO₂ catalysts due to unique physicochemical properties at the Pd-MO interface. Interestingly, the Pd_{PEG}@ZrO₂ catalyst showed the most promising activity for CO oxidation (regardless of pretreatment temperature) resulting from changes in the Pd oxidation state. In addition, the reported results indicated that the active sites in the amorphous structure (Pd_{PEG}@ZrO_{2-amorphous}) were significantly more active at low temperatures, presenting catalytically interesting systems for oxidation reactions under mild conditions. Moreover, CO DRIFTS findings indicate that Pd redispersion occurred under CO oxidation reaction conditions in the Pd_{PEG}@TiO₂ system, with potential formation of smaller Pd NPs, Pd clusters and oxidized Pd species postreaction. In the case of Pd_{PEG}@ZrO₂ and Pd_{PEG}@CeO₂, no evidence of Pd redispersion was observed during in-situ CO DRIFTS experiment. To better understand the reaction mechanism by which CO oxidation occurs over the surface of Pd_{PEG}@ZrO₂, XAS studies and other surface characterization techniques will be performed as part of future work for this investigation. The data presented here indicate that several phases may exist. The effect from the presence of monometallic Pd or PdO clusters is also not unlikely and cannot be excluded either. The conditions of the catalyst pretreatment, the state of the active Pd species, and the interaction between Pd and MO at the interface contribute to the enhanced catalytic performance in the case of Pd@ZrO2 under the considered CO oxidation conditions.

Conflicts of interest

There are no conflicts to declare.

Acknowledgements

The authors acknowledge support from the National Science Foundation for funding this research through collaborative research grants CHE-1900176/1900183. We also thank the Lumigen Instrument Center at Wayne State University for the use of the X-ray diffraction/spectroscopy (National Science Foundation MRI-1427926, MRI-1849578), electron microscopy facilities (National Science Foundation MRI-0216084). Part of this work was also performed at Stanford Synchrotron Radiation Lightsource (SSRL) of SLAC National Accelerator Laboratory, and the user of the SSRL is supported by the U.S. Department of Energy, Office of Science, Office of Basic Energy Sciences under Contract No. DE-AC02-76SF00515 and by Co-ACCESS supported by the U.S. Department of Energy, Office of Basic Energy Sciences, Chemical Sciences, Geosciences, and Biosciences Division. The authors acknowledge the technical support from the Michigan Center for Materials Characterization in the College of Engineering at University of Michigan.

References

- A. J. Maynes, D. M. Driscoll, P. A. DeSario, J. J. Pietron, A. M. Pennington, D. R. Rolison and J. R. Morris, *The Journal of Physical Chemistry C*, 2020, 124, 21491–21501.
- H. J. Kim, M. G. Jang, D. Shin and J. W. Han, ChemCatChem, 2020, 12, 11–26.
- S. M. McClure and D. W. Goodman, Chemical Physics Letters, 2009, 469, 1–13.
- 4 Y. Zhou, Z. Wang and C. Liu, Catalysis Science and Technology, 2015, 5, 69–81.
- 5 W. W. Wang, W. Z. Yu, P. P. Du, H. Xu, Z. Jin, R. Si, C. Ma, S. Shi, C. J. Jia and C. H. Yan, ACS Catalysis, 2017, 7, 1313–1329.
- B. Qiao, A. Wang, X. Yang, L. F. Allard, Z. Jiang, Y. Cui,
 J. Liu, J. Li and T. Zhang, *Nature Chemistry*, 2011, 3, 634–641.
- 7 M. T. M. Koper, N. P. Lebedeva and C. G. M. Hermse, Faraday Discussions, 2002, 121, 301–311.
- 8 J. A. Rodríguez and J. Hrbek, *Surface Science*, 2010, **604**, 241–244.
- 9 R. Prasad and P. Singh, *Catalysis Reviews Science and Engineering*, 2012, **54**, 224–279.
- 10 S. Jones, Y. Ji and M. Crocker, *Catalysis Letters*, 2016, 146, 909–917.
- 11 C. H. Wu, C. Liu, D. Su, H. L. Xin, H. T. Fang, B. Eren, S. Zhang, C. B. Murray and M. B. Salmeron, *Nature Catalysis*, 2019, **2**, 78–85.
- 12 H. J. Freund, G. Meijer, M. Scheffler, R. Schlögl and M. Wolf, *Angewandte Chemie International Edition*, 2011, **50**, 10064–10094.
- 13 T. S. Nguyen, F. Morfin, M. Aouine, F. Bosselet, J. L. Rousset and L. Piccolo, *Catalysis Today*, 2015, 253, 106–114.
- 14 V. P. Santos, S. A. C. Carabineiro, P. B. Tavares, M. F. R. Pereira, J. J. M. Órfão and J. L. Figueiredo, *Applied Catalysis B: Environmental*, 2010, 99, 198–205.
- 15 L. Guczi, A. Beck, A. Horváth, Z. Koppány, G. Stefler, K. Frey, I. Sajó, O. Geszti, D. Bazin and J. Lynch, *Journal of Molecular Catalysis A: Chemical*, 2003, 204–205, 545–552.
- 16 S. Song, X. Wang and H. Zhang, NPG Asia Materials, 2015, 7, e179-18.
- 17 X. Zhai, C. Liu, Q. Chang, C. Zhao, R. Tan, H. Peng, D. Liu, P. Zhang and J. Gui, New Journal of Chemistry, 2018, 42, 18066–18076.
- 18 J. Ye, D. G. Cheng, F. Chen and X. Zhan, *Industrial and Engineering Chemistry Research*, 2019, **58**, 21972–21982.
- 19 L. Delannoy, S. Giorgio, J. G. Mattei, C. R. Henry, N. ElKolli, C. Méthivier and C. Louis, *ChemCatChem*, 2013, 5, 2707–2716.
- 20 V. Bratan, C. Munteanu, C. Hornoiu, A. Vasile, F. Papa, R. State, S. Preda, D. Culita and N. I. Ionescu, *Applied Catalysis B: Environmental*, 2017, **207**, 166–173.
- 21 J. Y. Luo, M. Meng, X. Li, X. G. Li, Y. Q. Zha, T. D. Hu, Y. N. Xie and J. Zhang, *Journal of Catalysis*, 2008, **254**, 310–324.
- 22 A. A. Shutilov, G. A. Zenkovets, I. Y. Pakharukov and I. P. Prosvirin, *Kinetics and Catalysis*, 2014, **55**, 111–116.
- 23 M. Farrag, M. K. Das, M. Moody and M. Samy El-Shall, ChemPhysChem, 2021, 22, 312–322.
- 24 L. Jin, B. Liu, S. S. Duay and J. He, *Catalysts*, 2017, 7.
- 25 X. Liu, Q. Zhang, P. Ning, Q. Liu, Z. Song and Y. Duan, *RSC Advances*, 2017, **7**, 41936–41944.

- 26 H. Jeong, J. Bae, J. W. Han and H. Lee, ACS Catalysis, 2017, 7, 7097–7105.
- 27 S. W. Kim, J. Park, Y. Jang, Y. Chung, S. Hwang, T. Hyeon and Y. W. Kim, *Nano Letters*, 2003, 3, 1289– 1291.
- 28 Y. Xu, J. Ma, Y. Xu, L. Xu, L. Xu, H. Li and H. Li, RSC Advances, 2013, **3**, 851–858.
- 29 X. Wang, D. Liu, J. Li, J. Zhen, F. Wang and H. Zhang, Chemical Science, 2015, 6, 2877–2884.
- 30 M. Cargnello, N. L. Wieder, T. Montini, R. J. Gorte and P. Fornasiero, *Journal of the American Chemical Society*, 2010, **132**, 1402–1409.
- 31 M. Cargnello, T. Montini, S. Polizzi, N. L. Wieder, R. J. Gorte, M. Graziani and P. Fornasiero, *Dalton Transactions*, 2010, **39**, 2122–2127.
- 32 S. H. Joo, J. Y. Park, C. K. Tsung, Y. Yamada, P. Yang and G. A. Somorjai, *Nature Materials*, 2009, **8**, 126–131.
- 33 J. Lu, B. Fu, M. C. Kung, G. Xiao, J. W. Elam, H. H. Kung and P. C. Stair, *Science*, 2012, **335**, 1205–1208.
- 34 M. Cargnello, J. J. Delgado Jaén, J. C. H. Garrido, K. Bakhmutsky, T. Montini, J. J. Calvino Gámez, R. J. Gorte and P. Fornasiero, *Science*, 2012, 337, 713–717.
- 35 C. Y. Seo, E. Yi, M. Nahata, R. M. Laine and J. W. Schwank, *Materials Letters*, 2017, **206**, 105–108.
- 36 J. Wang, M. Wang, M. Shen, J. Wang, G. Wei and H. Li, *Journal of Rare Earths*, 2014, **32**, 1114–1119.
- 37 K. Bakhmutsky, N. L. Wieder, M. Cargnello, B. Galloway, P. Fornasiero and R. J. Gorte, *ChemSusChem*, 2012, **5**, 140–148.
- 38 J. N. Park, A. J. Forman, W. Tang, J. Cheng, Y. S. Hu, H. Lin and E. W. McFarland, *Small*, 2008, **4**, 1694–1697.
- 39 S. Hinokuma, H. Fujii, M. Okamoto, K. Ikeue and M. Machida, *Chemistry of Materials*, 2010, 22, 6183–6190.
- 40 Y. Zheng, K. Li, H. Wang, Y. Wang, D. Tian, Y. Wei, X. Zhu, C. Zeng and Y. Luo, *Journal of Catalysis*, 2016, 344, 365–377.
- 41 J. Ye, Y. Xia, D. guo Cheng, F. Chen and X. Zhan, *International Journal of Hydrogen Energy*, 2019, **44**, 17985–17994.
- 42 C. Gao, F. Lyu and Y. Yin, *Chemical Reviews*, 2021, **121**, 834–881.
- 43 J. Zhang and J. W. Medlin, Surface Science Reports, 2018, **73**, 117–152.
- 44 J. Zhang, B. Wang, E. Nikolla and J. W. Medlin, Angewandte Chemie - International Edition, 2017, **56**, 6594–6598.
- 45 F. A. Harraz, S. E. El-Hout, H. M. Killa and I. A. Ibrahim, *Journal of Catalysis*, 2012, **286**, 184–192.
- 46 C. Luo, Y. Zhang and Y. Wang, Journal of Molecular Catalysis A: Chemical, 2005, 229, 7–12.
- 47 H. Chen, J. A. Cronin and R. D. Archer, *Inorganic Chemistry*, 1995, **34**, 2306–2315.
- 48 P. S. Gradeff, F. G. Schreiber, K. C. Brooks and R. E. Sievers, *Inorganic Chemistry*, 1985, **24**, 1110–1111.
- 49 M. L. Ojeda, J. M. Esparza, A. Campero, S. Cordero, I. Kornhauser and F. Rojas, *Physical Chemistry Chemical Physics*, 2003, **5**, 1859–1866.
- P. I. Ravikovitch, G. L. Haller and A. v. Neimark, Advances in Colloid and Interface Science, 1998, 76– 77, 203–226.
- 51 T. B. Bolin, T. Wu, N. Schweitzer, R. Lobo-Lapidus, A. J. Kropf, H. Wang, Y. Hu, J. T. Miller and S. M. Heald, *Catalysis Today*, 2013, **205**, 141–147.
- 52 B. Ravel and M. Newville, *Journal of Synchrotron Radiation*, 2005, **12**, 537–541.

- 53 P. D. Coan, C. A. Farberow, M. B. Griffin and J. W. Medlin, *ACS Catalysis*, 2021, **11**, 3730–3739.
- 54 B. Wang, J. Zhang, L. P. Herrera, J. W. Medlin and E. Nikolla, *Industrial and Engineering Chemistry Research*, 2019, **58**, 4032–4041.
- 55 K. S. W. Sing, D. H. Everett, R. A. W. Haul, L. Moscou, R. A. Pierotti, J. Rouquérol and T. Siemieniewska, *Pure and Applied Chemistry*, 1985, **57**, 603–619.
- 56 P. D. Burton, D. Lavenson, M. Johnson, D. Gorm, A. M. Karim, T. Conant, A. K. Datye, B. A. Hernandez-Sanchez and T. J. Boyle, *Topics in Catalysis*, 2008, 49, 227–232
- 57 X. Liu, A. Wang, X. Yang, T. Zhang, C. Y. Mou, D. S. Su and J. Li, *Chemistry of Materials*, 2009, **21**, 410–418.
- 58 L. F. de L. e Freitas, B. Púertolas, J. Zhang, B. Wang, A. S. Hoffman, S. R. Bare, J. Pérez-Ramírez, J. W. Medlin and E. Nikolla, ACS Catalysis, 2020, 10, 5202–5207.
- 59 Y. Zhou, D. E. Doronkin, M. Chen, S. Wei and J. D. Grunwaldt, *ACS Catalysis*, 2016, **6**, 7799–7809.
- 60 E. D. Park, S. H. Choi and J. S. Lee, *Journal of Physical Chemistry B*, 2000, **104**, 5586–5594.
- 61 E. Sasmaz, C. Wang, M. J. Lance and J. Lauterbach, *Journal of Materials Chemistry A*, 2017, **5**, 12998–13008.
- 62 E. J. Jang, J. Lee, D. G. Oh and J. H. Kwak, *ACS Catalysis*, 2021, **11**, 5894–5905.
- 63 N. C. Nelson, L. Chen, D. Meira, L. Kovarik and J. Szanyi, *Angewandte Chemie*, 2020, **132**, 17810–17816.
- 64 R. Ouyang, J. X. Liu and W. X. Li, Journal of the American Chemical Society, 2013, 135, 1760–1771.
- 65 Y. Q. Su, J. X. Liu, I. A. W. Filot and E. J. M. Hensen, *Chemistry of Materials*, 2017, **29**, 9456–9462.
- 66 G. S. Parkinson, Z. Novotny, G. Argentero, M. Schmid, J. Pavelec, R. Kosak, P. Blaha and U. Diebold, *Nature Materials*, 2013, 12, 724–728.
- 67 D. Tessier, A. Rakai and F. Bozon-Verduraz, Spectroscopic Study of the Interaction of Carbon Monoxide with Cationic and Metallic Palladium in Palladium-Alumina Catalysts, 1992, vol. 88.
- 68 J. T. Grant, C. A. Carrero, A. M. Love, R. Verel and I. Hermans, *ACS Catalysis*, 2015, **5**, 5787–5793.
- 69 M. Faticanti, N. Cioffi, S. de Rossi, N. Ditaranto, P. Porta, L. Sabbatini and T. Bleve-Zacheo, *Applied Catalysis B: Environmental*, 2005, **60**, 73–82.
- 70 H. Zhu, Z. Qin, W. Shan, W. Shen and J. Wang, *Journal of Catalysis*, 2005, **233**, 41–50.
- 71 X. Zhang, H. Shi and B.-Q. Xu, *Angewandte Chemie*, 2005, **117**, 7294–7297.
- 72 S. Sharma, S. Hilaire, J. M. Vohs, R. J. Gorte and H. W. Jen, *Journal of Catalysis*, 2000, **190**, 199–204.
- 73 P. Claus, A. Bruckner, C. Mohr and H. Hofmeister, Journal of the American Chemical Society, 2000, 122, 11430–11439.
- 74 S. M. Stagg, E. Romeo, C. Padro and D. E. Resasco, *Journal of Catalysis*, 1998, **178**, 137–145.
- 75 H. Jeong, J. Bae, J. W. Han and H. Lee, ACS Catalysis, 2017, 7, 7097–7105.
- 76 S. J. Tauster, S. C. Fung, R. T. K. Baker and J. A. Horsley, *Science*, 1981, **211**, 1121–1125.
- 77 S. Zhang, P. N. Plessow, J. J. Willis, S. Dai, M. Xu, G. W. Graham, M. Cargnello, F. Abild-Pedersen and X. Pan, *Nano Letters*, 2016, **16**, 4528–4534.
- 78 A. Satsuma, K. Osaki, M. Yanagihara, J. Ohyama and K. Shimizu, Applied Catalysis B: Environmental, 2013, 132–133, 511–518.

79 C. Chen, Y. Yeh, M. Cargnello, C. B. Murray, P. Fornasiero and R. J. Gorte, ACS Catalysis, 2014, 4, 3902–3909.